Targeted delivery of inhalable drug particles in a patient-specific tracheobronchial tree with moderate COVID-19: A numerical study

Jianwei Wang [a], Ya Zhang [b], Xiaole Chen [a,*], Yu Feng [c], Xiaoyong Ren [b], Minjuan Yang [b], Ting Ding [a]

[a] School of Energy and Mechanical Engineering, Nanjing Normal University, Nanjing, Jiangsu 210046, China
[b] Department of Otolaryngology Head and Neck Surgery, The Second Affiliated Hospital of Xi'an Jiaotong University, Xi'an, Shaanxi 710004, China
[c] School of Chemical Engineering, Oklahoma State University, Stillwater, OK 74078, USA

ARTICLE INFO

ABSTRACT

The coronavirus disease 2019 (COVID-19) pandemic has led to severe social and economic disruption worldwide. Although currently no consent has been reached on a specific therapy that can treat COVID-19 effectively, several inhalation therapy strategies have been proposed to inhibit SARS-CoV-2 infection. These strategies include inhalations of antiviral drugs, anti-inflammatory drugs, and vaccines. To investigate how to enhance the therapeutic effect by increasing the delivery efficiency (DE) of the inhaled aerosolized drug particles, a patient-specific tracheobronchial (TB) tree from the trachea up to generation 6 (G6) with moderate COVID-19 symptoms was selected as a testbed for the in silico trials of targeted drug delivery to the lung regions with pneumonia alba, i.e., the severely affected lung segments (SALS). The 3D TB tree geometry was reconstructed from spiral computed tomography (CT) scanned images. The airflow field and particle trajectories were solved using a computational fluid dynamics (CFD) based Euler-Lagrange model at an inhalation flow rate of 15 L/min. Particle release maps, which record the deposition locations of the released particles, were obtained at the inlet according to the particle trajectories. Simulation results show that particles with different diameters have similar release maps for targeted delivery to SALS. Point-source aerosol release (PSAR) method can significantly enhance the DE into the SALS. A C++ program has been developed to optimize the location of the PSAR tube. The optimized simulations indicate that the PSAR approach can at least increase the DE of the SALS by a factor of 3.2× higher than conventional random-release drug-aerosol inhalation. The presence of the PSAR tube only leads to a 7.12% change in DE of the SALS. This enables the fast design of a patient-specific treatment for reginal lung diseases.

© 2022 Published by Elsevier B.V.

1. Introduction

Coronavirus disease 2019 (COVID-19) is highly infectious, causing acute respiratory distress syndrome [1]. The severe symptoms, including dyspnea, fever, and acute inflammatory lung injury, have been reported in approximately 15.7% of patients with COVID-19 [2]. Specifically, SARS-CoV-2 virus can penetrate into the deeper lung, causing consolidation and ground glass infiltration of lung tissue, resulting in high mortality rate [3,4]. COVID-19 vaccines can reduce the risk of getting and spreading the virus, and offer life-saving protections by reducing the death rate caused by SARS-CoV-2 infection [5]. Although COVID-19 vaccination rates increase around the world, COVID-19 vaccination progress is only 41.7% for the fully vaccinated population worldwide as of December 20th 2021 [6]. It is still not close to 60–70% when herd immunity can be possibly achieved, beside for the resurgence of the pandemic because of the COVID-19 Delta variant and Omicron variant which are more infectious. Therefore, seeking effective treatments for COVID-19 patients is still of great interest.

Inhalation therapy was considered a standard method of treatment for various respiratory diseases, especially for chronic obstructive pulmonary disease (COPD) [7,8]. It delivers drugs directly to the affected area [9]. This method was also used to treat COVID-19 [10–12]. For example, Yu et al. [13] and Sahakijpijarn et al. [14] proposed the treatment of COVID-19 via inhaling budesonide and remdesivir, respectively. However, the distribution of affected lung segments in COVID-19 patient caused by bronchial obstruction and fibrosis showed segmental, irregular, and nodal characteristics [1,15]. Thus, the effective treatment strategy for COVID-19, tuberculosis and lung cancer is to deliver highly concentrated drugs to the specific lesion areas [16,17]. Unfortunately, conventional inhalation drug delivery methods lead to relatively low drug deposition efficiency in the affected regions due to non-directional delivery. [18,19]. Meanwhile, the inhalable drugs can also have systemic side effects on human body [20–22]. Therefore, it is

* Corresponding author.
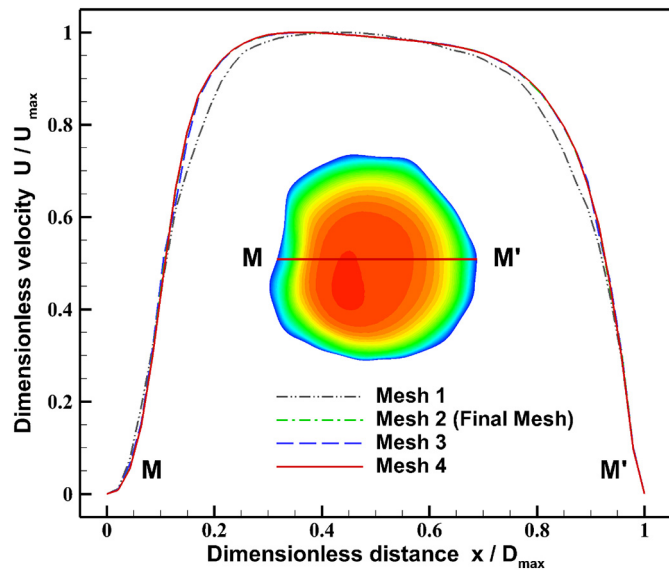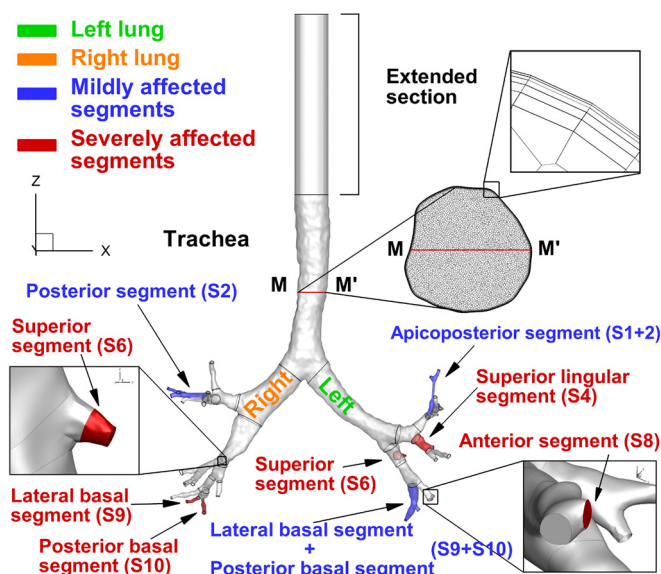 *E-mail address:* xlc@njnu.edu.cn (X. Chen).

Fig. 1. Schematics of the tracheobronchial (TB) tree geometry (trachea to G6) of a patient with moderate COVID-19.

Fig. 2. Comparisons of the dimensionless velocity profiles along line M-M' of meshes with different mesh cell numbers.

necessary to develop novel inhalation therapies to improve drug delivery efficiency in specific lung segments.

In the last two decades, efforts have been made to optimize the delivery efficiency of drug aerosols to the lungs. For example, controlling aerodynamic particle diameter and inhalation pattern [23–25] are beneficial for these whole lung diseases [26]. Therefore, adjusting powder properties, such as size, density, and composition, for the dry powder inhalers can improve the overall delivery efficiency of the drug powder to deeper lung regions [27–31]. Magnetic aerosols were employed to achieve targeted aerosol delivery to desired lung areas [32,33]. Kleinstreuer et al. [34] proposed a controlled air-particle stream method to achieve site-specific targeted drug delivery based on changing the particle release position. Yousefi et al. [35] proposed a smart spacer concept using a one-way valve. Controlled condensational growth can also achieve site-specific deposition in the airway [36]. Traveling through the human respiratory system via oral inhalation, particles mainly deposited in the pharynx and larynx due to inertial impaction and secondary flow dispersion [37–40]. Moreover, turbulent laryngeal jet and the waked recirculation flows in the trachea were generated as the airflow passing through the glottis [41,42]. Such flow structures can lead to high deposition efficiencies of drug aerosols in human upper airway and insufficient deposition of drug aerosols in the lower airways (<25%) [43–45]. To enhance the drug delivery efficiency to lower airways, catheters or bronchoscopes could be used to instill the drug aerosols in pulmonary sites that are closer to the lower airways, avoiding the loss of drugs due to the deposition in upper airways [46,47]. Specifically, Kim et al. [48] proposes a method to instill microvolume liquid plugs into the specific bronchial tree through a glass capillary tube, which allows precise dose control for targeted delivery. Similarly, an intracorporeal nebulizing catheter was used to deliver chemotherapy drugs to lobe-specific to improve the targeted deposition of drugs [49,50]. The

Table 2
Airflow and particle parameters.

Parameters	Values
Flow rate [L/min]	15
Flow temperature [K]	310.15
Mean velocity at the trachea inlet [m/s]	1.003
Average Reynolds number at the trachea inlet	1027
Air density [kg/m^3]	1.139
Air dynamic viscosity [kg/m·s]	2.002×10^{-5}
Particle density [kg/m^3]	1000
Particle diameter [μm]	1 to 25
Stokes number	0.00016 to 0.09761

effective delivery to specific lung lobes was achieved by a regionally targeted device in a 3D-printed in vitro lung model [51].

Although there are existing research efforts on targeted pulmonary drug delivery as mentioned above, the effectiveness of such inhalation

Fig. 3. Comparison of the deposition fractions in the SALS with different numbers of particles.

Table 1
Details of the meshes used for mesh independence test.

| Mesh No.	Total number of elements
1	1,095,643
2 (final)	2,921,397
3	5,363,711
4	16,910,282

therapy strategies on treating COVID-19 patients has not been discussed. Therefore, the objective of this study is to numerically explore the possibility of enhancing the particle delivery efficiency (DE) in specific lung segments of a patient with moderate COVID-19 infection using the proposed drug delivery method, i.e., point-source aerosol release (PSAR). Specifically, the airflow and particle trajectories were solved by a computational fluid dynamics (CFD) based Euler-Lagrange method at an inhalation flow rate of 15 L/min. Drug particle release maps, which record the particle deposition sites, were obtained at the trachea inlet according to the particle trajectories. A C++ program was developed to optimize the position of the PSAR tube for enhancing the total DE of severely affected segments in the left and right lungs. The influence of the PSAR tube presence on the airflow field and DEs in different lung segments was also compared with cases without the PSAR tube. This

method is ready to be extended for other targeted drug-aerosol delivery applications, e.g., inhalation therapy for lung cancer [52,53].

2. Geometry and mesh

The geometry of the patient-specific tracheobronchial (TB) tree was constructed from spiral computed tomography (CT) scanned images of a patient with moderate COVID-19. The CT scan was taken when the patient was being hospitalized.

The TB tree geometry, as shown in Fig. 1, consists of airways from the trachea up to generation 6 (G6). According to the spiral CT images, severe pneumonia can be found in the superior lingular segment (S4), superior segment (S6) and anterior segment (S8) of the left lung and the superior segment (S6), lateral basal segment (S9), and posterior basal
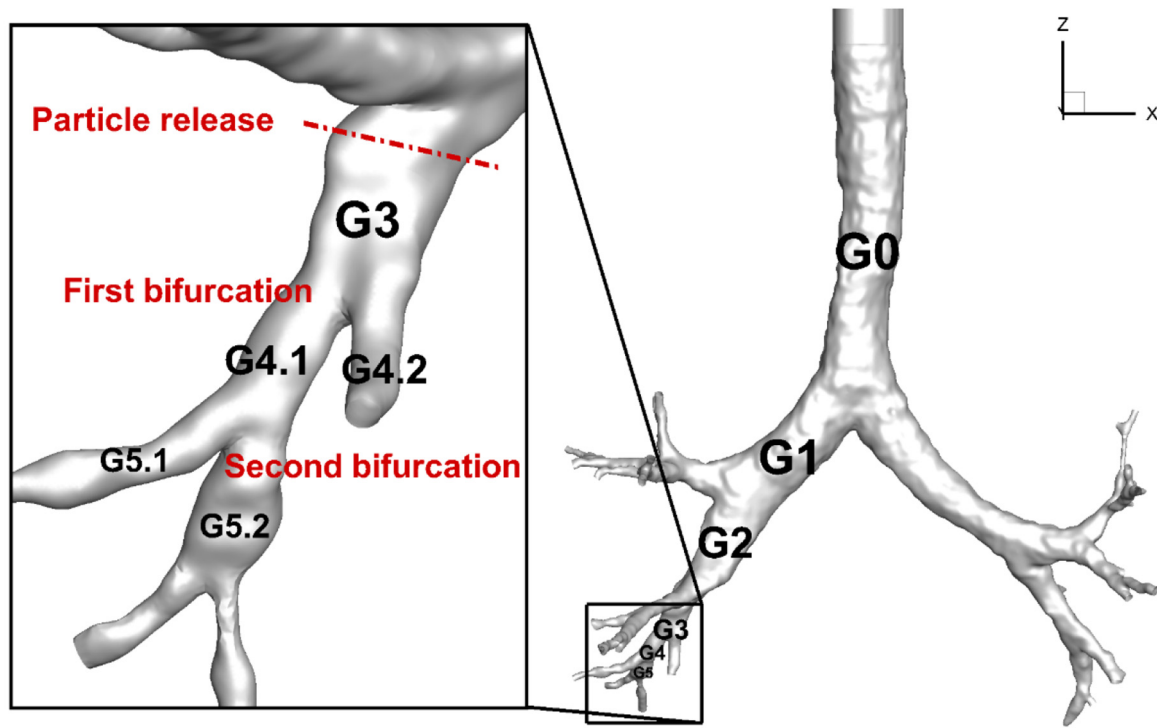
(a) Schematic of the segment of G3-G5 airway selected from the TB tree model
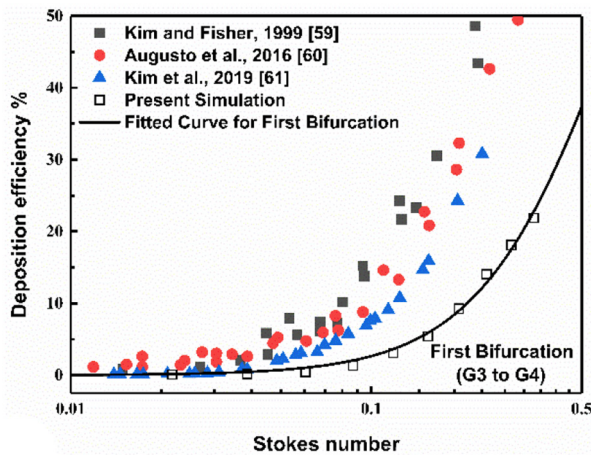
(b) First bifurcation
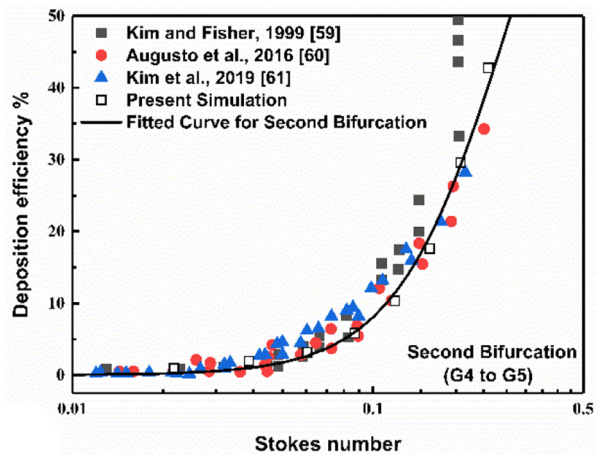
(c) Second bifurcation

Fig. 4. Comparison of the deposition efficiency between the patient-specific TB tree and previous published data.

segment (S10) of the right lung. The severe pneumonia regions which are colored in red in Fig. 1, are the designated lung sites for the targeted drug delivery in this study. The segments with mild pneumonia, including apicoposterior segment (S1 + 2), lateral basal segment (S9), posterior basal segment (S10) of the left lung, and posterior segment (S2) of the right lung, are colored in blue in Fig. 1. The rest lung segments, which had no evident signs of pneumonia, were considered healthy. To evaluate the effect of the presence of the tube for PSAR on the particle flow, the inlet of the trachea was extended with a length equal to 5 times the hydraulic diameter of the trachea inlet, which simulates the catheter of the tracheal intubation.

A Mesh independence test was performed before particle transport and deposition simulations. Four polyhedron-based meshes with different total cell numbers were generated using Ansys Fluent Meshing. Mesh details can be found in Table 1. Each mesh contained five near-wall prism layers, as shown in Fig. 1. The dimensionless velocity profiles along line M-M' across the trachea (see Fig. 1) were compared with the four meshes at the inhalation flow rate of 15 L/min. The maximum percentage difference between the velocity profiles using Mesh 2 and Mesh 4 was less than 5% (see Fig. 2). Thus, Mesh 2 was selected as the final mesh employed in the simulations.

3. Methodology

3.1. Governing equations for continuous phase

For a patient with a steady-state breathing rate of 15 L/min, the Reynolds number at the inlet of the trachea is 1027. Therefore, the airflow in the TB tree is laminar. Due to the limited pressure variations in the airway, the flow field was assumed to be incompressible. Accordingly, the governing equations for the conservation of mass and momentum of the incompressible viscous laminar airflow can be given as:

$$\nabla \cdot \vec{u} = 0 \tag{1}$$

$$\frac{\partial \vec{u}}{\partial t} + \left(\vec{u} \cdot \nabla \right) \vec{u} = -\frac{\nabla p}{\rho} + \nabla \cdot \left[\upsilon \left(\nabla \vec{u} + \left(\nabla \vec{u} \right)^{tr} \right) \right] \tag{2}$$

where $\vec{u}$ is the air velocity; t is the time; p is the air pressure; ρ is the air density; υ is the kinematic viscosity of air and $\left(\nabla \vec{u} \right)^{tr}$ is the transpose of $\nabla \vec{u}$.

3.2. Governing equations for discrete phase

The aerodynamic diameter is a crucial factor affecting the spatial distribution of particles deposition and drug delivery efficiency. Large particles (>6 μm) are mainly deposited in the upper airways, while particles with diameters between 2 and 6 μm are more suitable for treating the central and small airways [54]. Thus, this study focuses on the micrometer particles. Assuming the particle suspension in the airway is dilute, the movement and deposition of micrometer particles in the lower airways are mainly influenced by gravity and drag force [55]. Thus, the simplified particle translation equation can be given as:

$$m_p \frac{d\vec{u}_p}{dt} = \frac{1}{8} \pi \rho d_p^2 C_{Dd} \left(\vec{u} - \vec{u}_p \right) \left| \vec{u} - \vec{u}_p \right| + m_p \vec{g} \tag{3}$$

where m_p, $\vec{u}_p$ and d_p are the particle mass, velocity and diameter, respectively; C_{Dd}, the drag coefficient of the particle, is given as [56]:

$$C_{Dd} = \frac{a_1}{\text{Re}_p} + \frac{a_2}{\text{Re}_p^2} + a_3 \tag{4}$$

where a_1, a_2, a_3 are coefficients determined by the particle Reynolds number Re_p, which is defined as:

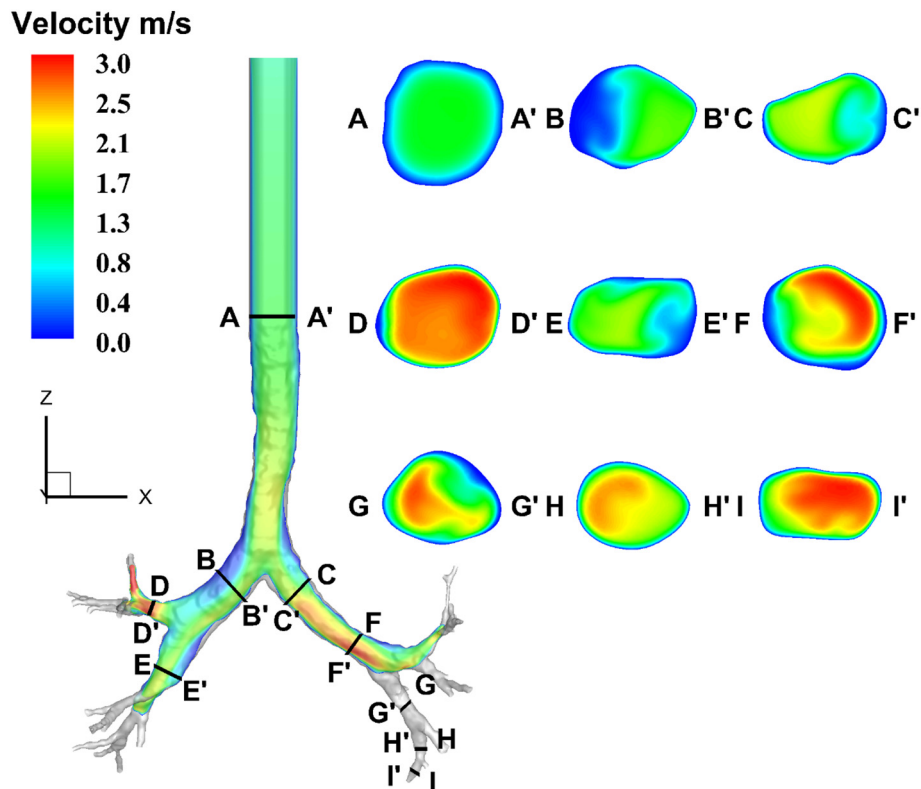$$\text{Re}_p = \frac{\rho \left| \vec{u} - \vec{u}_p \right| d_p}{\mu} \tag{5}$$

Fig. 5. Velocity distribution of the lower airway of the moderate COVID-19 patient at the inhalation flow rate of 15 L/min.

3.3. Numerical setup

Steady-state simulations were executed at an inhalation flow rate of 15 L/min. The average velocity at the inlet of the trachea was 1.003 m/s. In light of dilute particle suspensions, a one-way coupled Euler-Lagrange model was employed to track the particle transport and deposition. To obtain the correlations between DE and the particle Stokes number, particles with diameters from 1 to 25 μm were simulated. The details of the airflow and particle parameters are summarized in Table 2. For each simulation, 10, 000 particles were released at random locations on the inlet for the regular case or in the PSAR tube for the targeted delivery case. As shown in Fig. 3, increasing the number of released particles to 30, 000 at the inlet only leads to a change of 0.89% in DF in the SALS for 7.5 μm particles.

The initial velocity of the particle was assumed to be the same as the velocity of the local airflow. Considering the existence of the airway mucus layer, it was assumed that deposition occurred when particles contact the airway wall boundaries. Particles that escaped from the outlets were regarded as delivering into the lung segments accordingly.
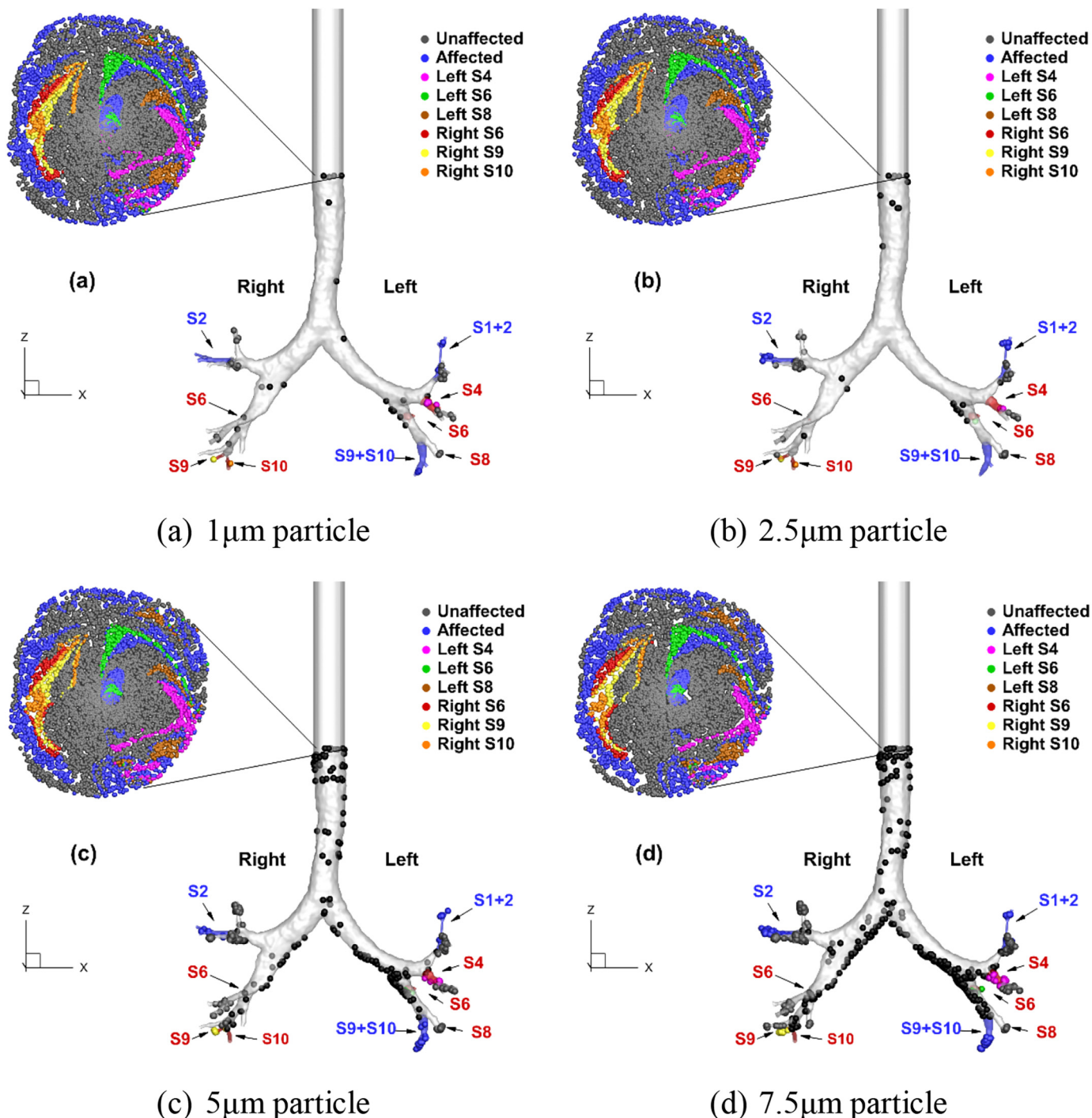

(a) 1μm particle

(b) 2.5μm particle

(c) 5μm particle

(d) 7.5μm particle

Fig. 6. Release maps and final deposition locations of particles with different diameters in the patient-specific TB tree.
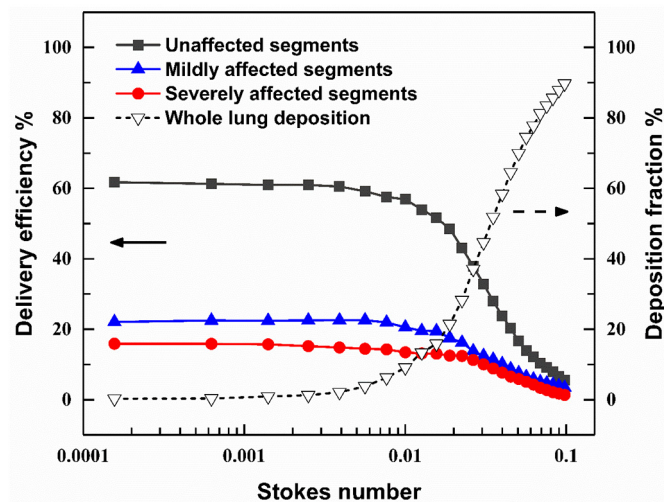
Fig. 7. Delivery efficiencies of the particles in different lung segments and deposition fractions in the patient-specific TB tree.

Table 3
Delivery efficiency parameters for different lung segments with a 4 mm PSAR tube.

Particle diameter (μm)	Delivery efficiency (%)					
	Left lung			Right lung		
	SALS	MALS	ULS	SALS	MALS	ULS
1	51.12	29.11	19.64	75.94	9.22	14.74
2.5	51.31	28.01	20.43	75.81	8.85	15.16
5	45.36	16.03	37.82	68.84	7.49	17.41
7.5	42.25	10.11	39.04	63.56	5.99	19.36

4. Results and discussion

4.1. Model validations

The study of particle deposition in the pulmonary airways is quantified in terms of the deposition fraction (DF) [57]. The DF is defined as:

$$DF = \frac{m_d}{m_t} \times 100\% \qquad (6)$$

where m_d is the total mass of deposited particles, and m_t is the total mass of inhaled particles.

(a) 1μm particle

(b) 2.5μm particle

(c) 5μm particle
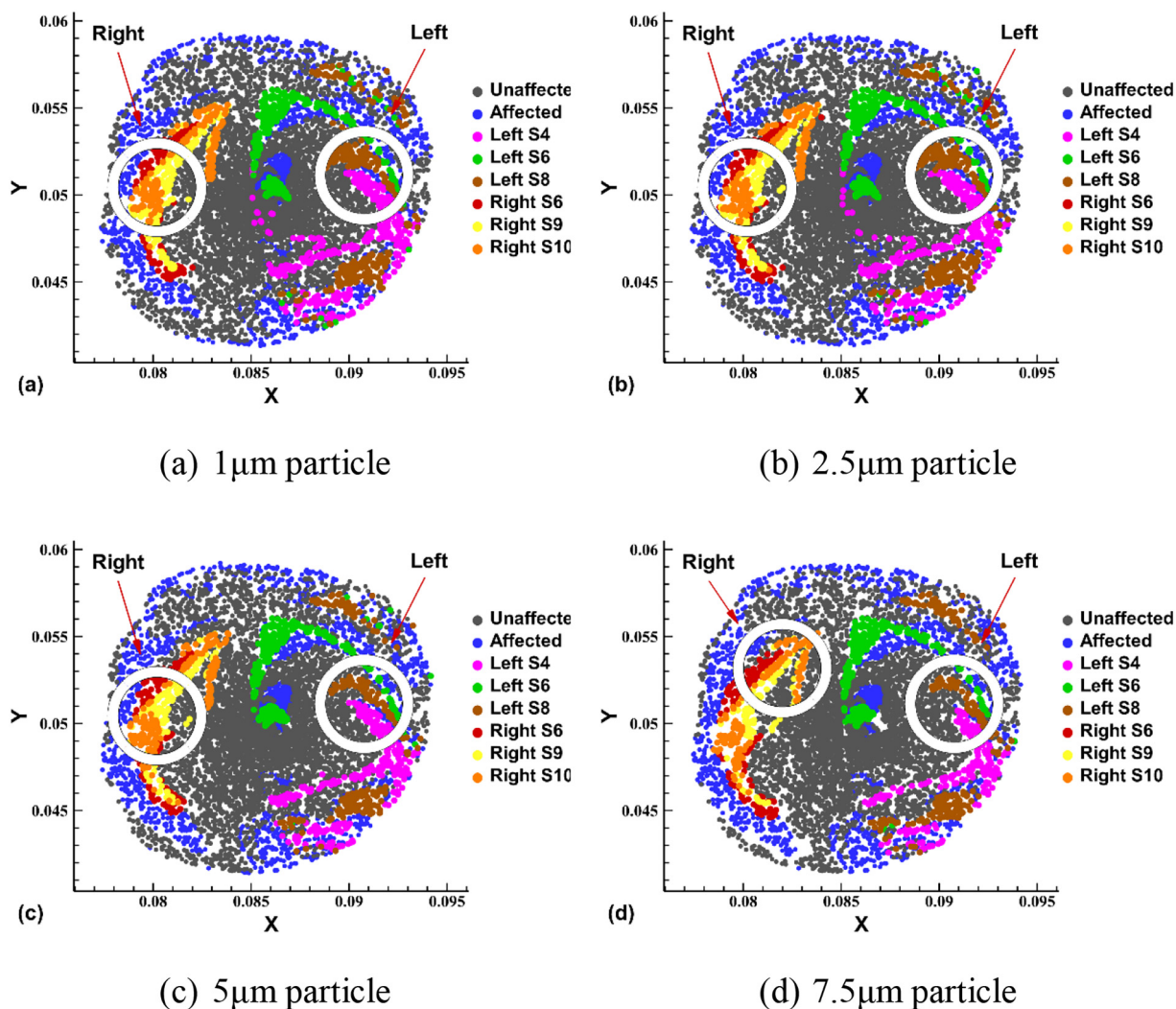

(d) 7.5μm particle

Fig. 8. The optimal PSAR tube position for the left and right lungs for different particle sizes.

To evaluate the importance of particle inertia in pulmonary airflow, Stokes number (Stk), a dimensionless parameter, can be introduced. In this study, Stk is defined as [27,58]:

$$Stk = \frac{\rho_p d_p^2 U_{in}}{18 \mu D_{in}} \tag{7}$$

where U_{in} is the average inlet airflow velocity; D_{in} is the inlet diameter.

To validate the particle transport and deposition model, a segment of the G3 to G5 (see Fig. 4(a)) airway was selected from current model to compare the particle deposition efficiencies in the G3 to G5 airway models [59–61]. In general, the deposition efficiencies of the particles in the TB tree model showed similar trends at the first bifurcation (see Fig. 4(b)) and the second bifurcation (see Fig. 4(c)) with previous experimental and numerical results [59–61]. The discrepancies could be attributed to the flow rate and the inter-subject variabilities of the pulmonary airway anatomy. Predictions of particle transport and deposition in the human respiratory system have been validated in our previous study [62–64].

4.2. Airflow distributions

The airflow field, including the velocity and pressure distributions in ideal, obstructed, and realistic pulmonary models, has been analyzed by numerous previous studies [38,62,65]. The air velocity contours in the coronal plane and nine cross-sectionals of the COVID-19 patient airway are shown in Fig. 5. The velocity is higher in the center of the trachea at cross-sections A-A'. The highest velocity magnitude is 1.28 m/s. The

incoming airflow from the inlet splits at the bifurcation of the trachea resulting in the skewed velocity profile in the main bronchus (i.e., cross-sections B-B′ and C-C′ in Fig. 5) [66]. The velocity magnitude increases to 2.25 m/s. Thus, the maximum axial velocity of airflow inclines to the inner wall of the main bronchus. The secondary flow moves along the main bronchus wall from the high-velocity flow region at the inner wall side to the low-velocity flow region at the lateral wall side (i.e., cross-section E-E', G-G' and H-H′ in Fig. 5) [67]. Due to the reduction of lumen area, the airflow velocity reaches 2.94 m/s and 2.98 m/s at cross-section D-D′ and I-I′, respectively.

4.3. The relationship between the final deposition location and the particle release map

Fig. 6 compares the particle release maps (see the upper left part in each subfigure) and the final deposition distributions of particles in the airway (see the right part in each subfigure) for particles with different diameters, i.e., 1 μm, 2.5 μm, 5 μm and 7.5 μm. As shown in Fig. 6(a) to (d), the number of particles deposited enhances with the increase of particle diameter. It can be found that with the increase in particle size, concentrated deposition of the particles that occurs near the carina ridge of the bifurcation becomes more significant due to the enhanced inertial impaction effect [68,69]. Specifically, induced by the skewed airflow velocity distributions and resultant flow separations near the bifurcation, higher velocity impingement occurs near the inner side of the tube wall downstream to the bifurcating point (see B-B′ and C-C′ in Fig. 5) [70,71]. Therefore, the particles carried by the airflow tend to

(a) PSAR tube for the left lung
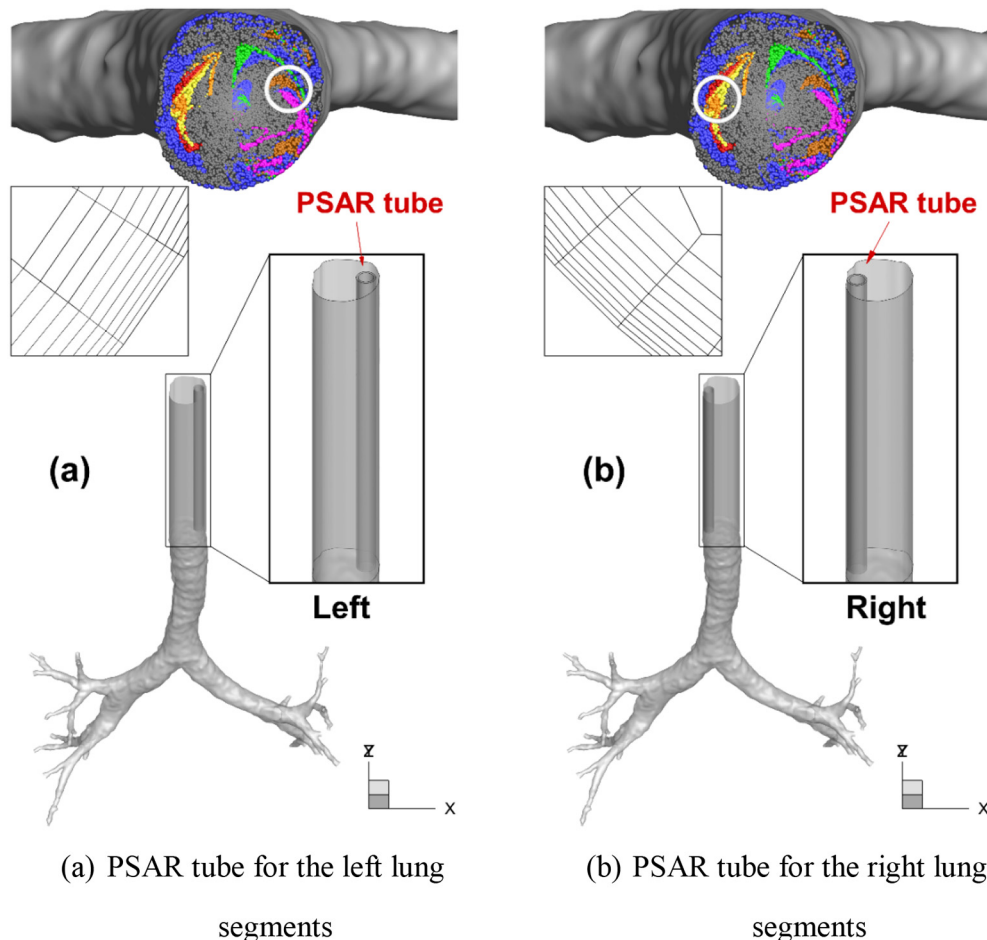segments

(b) PSAR tube for the right lung
segments

Fig. 9. Geometries of the reconstructed pulmonary airways with PSAR tubes optimized for 2.5 μm particles.

impact and deposit on the inner side of the airway walls downstream to the bifurcating point.

As shown in the left part of Fig. 6(a) to (d), the deposition locations of the particles are illustrated in the particle release map using different colors. The non-deposited particles are grouped into three categories, i.e., (1) particles (colored dots except the blue and gray ones in Fig. 6) entering the severely affected lung segments (SALS), (2) blue particles entering the mildly affected lung segments (MALS), and (3) gray particles entering the unaffected lung segments (ULS). In general, particles released from the left and right side of the trachea at the inlet enter the left and right lung airways, respectively. However, the available regions for drug delivery to SALS in the release maps are highly irregular and asymmetrical. Furthermore, the void area increases in the release map with the increase in particle diameter. Such an observation

(a) Velocity distributions contours for left PSAR tube

(b) Velocity distributions contours for right PSAR tube

Fig. 10. Velocity distributions of the pulmonary airflow fields with PSAR tube.

indicates that with larger particle size, more particles deposited in the TB tree form the trachea to G6 instead of traveling into deeper lung segments. This observation can also be supported by the comparisons of particle deposition patterns shown in Fig. 6(a) to (d). It can also be observed from Fig. 6(a) to (d) that the available particle release regions to achieve targeted drug delivery to SALS and MALS are highly consistent among particles with different diameters. It indicates that regional targeted drug release for SALS and MALS by COVID-19 could be achieved with good tolerance on the particle size. Similar conclusions were also obtained for lobe-targeted drug delivery in the literature [34,51].

4.4. Deposition fraction and delivery efficiency

To quantify particles delivered to the specific lung segments, the delivery efficiency (DE) is defined as:

$$DE = \frac{m_e}{m_t} \times 100\% \tag{8}$$

where m_e is the total mass of particles entering a specific region.

It is worth mentioning that the abbreviation DE used in this study refers to delivery efficiency rather than deposition efficiency, which is often used in literature. Even though the inhalation flow rate is fixed at 15 L/min, the results of this study still cover a wide range of the Stokes number. Thus, the DE and particle trajectories could be used to estimate the conditions with different flow rates or transient inhalation in general [67,71].

Fig. 7 depicts the variations of DF and DEs for different types of lung segments, i.e., SALS, MALS, and ULS, as a function of Stokes number (Stk). The general trend of the DF curve (see the dashed line in Fig. 7) of the particles is similar to the previous studies [59,67,72]. The DF of the particles increases with the increase of Stk, and has a steep slope in Stk ranging from 0.005 to 0.1. Specifically, the increase in inertial impaction effect noted by the increase in Stk is the main mechanism that caused the increase in DF in the TB tree. Such an observation is aligned with the localized deposition patterns shown in Fig. 6(a) to (d).

DEs (see solid lines in Fig. 7) for different lung segments changed slightly (<1%) at Stk < 0.0056. It means the light particles could follow the airflow across the airway to the deeper lung segment. The DEs (see solid lines in Fig. 7) for different lung segments all decrease with the increase of the Stk due to the inertial impact of the particles. However, the numbers of particles delivered into different segments are different. For example, only 15.89% of 2.5 μm particles (see the red line with circles in Fig. 7) and 22.08% of them (blue line with triangles in Fig. 7) successfully enter the SALS and MALS, respectively. The rest of the 2.5 μm particles, i.e., 62.03%, are delivered into ULS, where are not the designated lung sites for the drug delivery. To enhance the therapeutic effect and reduce the potential side effect due to the drug deposition on healthy tissues [22], the transport of that 62.03% of the inhaled drugs could be better modulated and delivered to SALS and MALs. To enhance the effective drug delivery to SALS and MALS, the PSAR approach is proposed and further analyzed to achieve the targeted drug delivery goal.
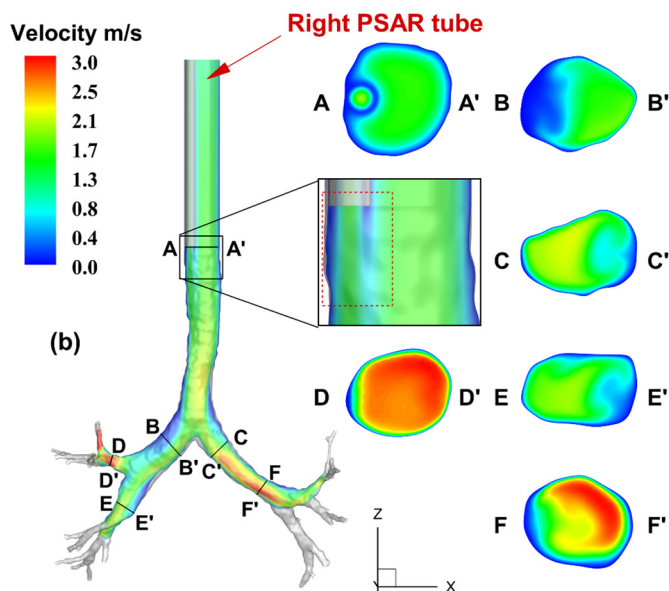
Table 4

Average volumetric flow rates for different lung segments without and with the PSAR tube.

Presence of the PSAR tube	Flow rate (L/min)		
	Lung segment types		
	SALS	MALS	ULS
Without PSAR tube	3.203	2.786	9.011
With PSAR tube	3.200	2.792	9.008
Relative error (%)	0.082	0.216	0.038
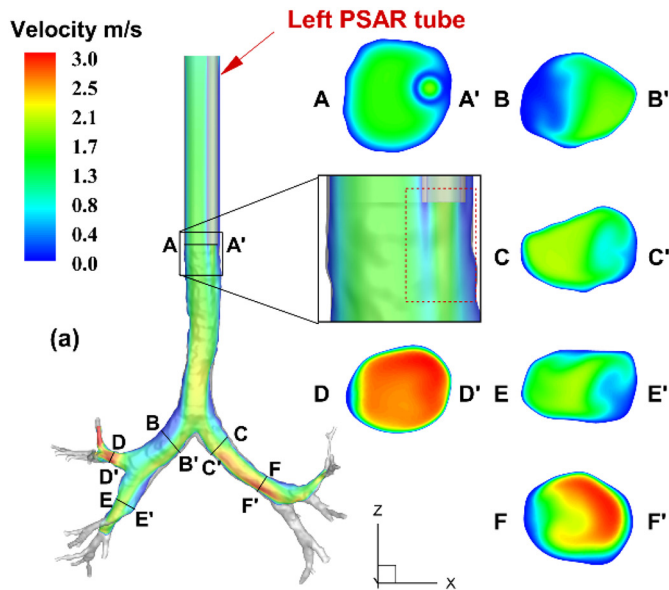
(a) 1μm particle

(b) 2.5μm particle

(c) 5μm particle
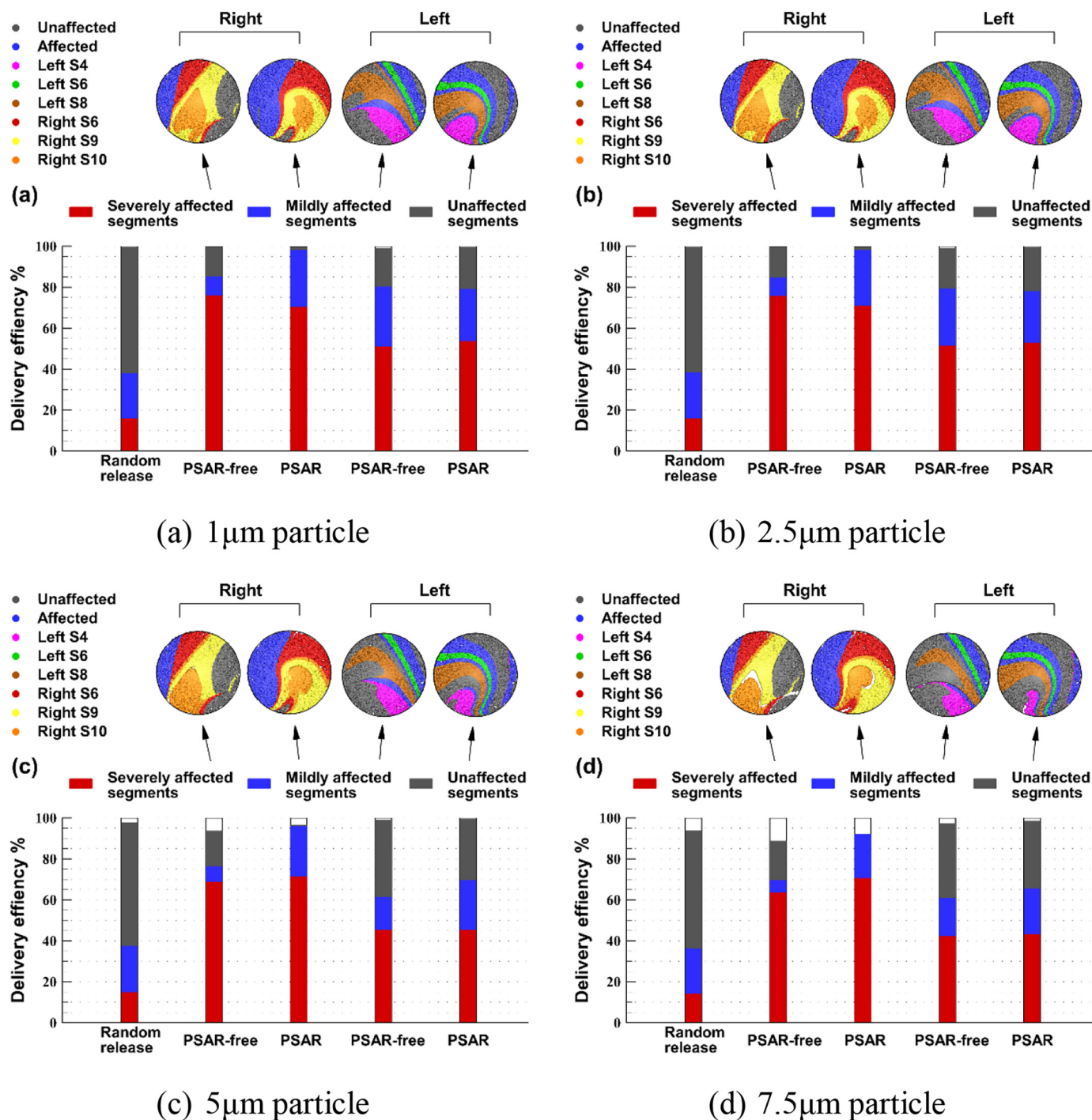

(d) 7.5μm particle

Fig. 11. Comparisons of the particle release maps and DEs between the simulations with and without PSAR tube as well as random-release simulation for different particle diameters.

4.5. Point-source aerosol release (PSAR) and optimization

Although lobe-specific pulmonary drug delivery has been studied and approved feasible [51], it is more challenging to realize the targeted delivery to smaller designated lung sites, i.e., specific lung segments. Therefore, it is necessary to systematically investigate and determine the PSAR tube location to release drugs and target specific lung segments, i.e., SALS and MALS. Specifically, there are two requirements to be fulfilled, i.e., (1) the particles released from the PSAR tube need to cover all SALS caused by SARS-CoV-2 infection either in the left or right lung; and (2) the diameter and wall thickness of the PSAR tube

need to be realistic for manufacturing purpose and clinical practice. The PSAR tube was aligned with the trachea inlet to simulate the case of the targeted drug-aerosol release in intubated patients.

To optimize the location of the PSAR tube as the drug release position, the release maps at the trachea inlet for the particles with different diameters were obtained first (see Fig. 8). For post-processing, a C++ program was developed to seek the optimal position and diameter of the PSAR tube based on the release maps. Specifically, the C++ program looped through the positions in the XY plane to find the top 10 coordinates that have the highest DE in the SALS for a given PSAR tube diameter. Coordinates that could cover only one or two SALS were

discarded. The program also looped through different PSAR tube diameters from 2 mm to 8 mm. The optimized results, as shown in Fig. 8, suggest that a 4 mm PSAR tube can achieve a much higher DE in SALS. DEs corresponding to the optimal position of the 4 mm PSAR tube (see Fig. 8 (a) to (d)) for different lung segments are summarized in Table 3. In contrast, DEs of the particles in SALS are lower than 20% (see Fig. 7), if the particles are randomly released. This optimized PSAR tube location also has limited change under different particle size conditions. Therefore, a PSAR tube with a 4 mm inner diameter and a wall thickness of 1 mm was selected for the following analysis. It is worth mentioning that the effect of the PSAR tube on the airflow field and particle trajectories are still not considered yet.

4.6. Airflow distributions with the PSAR tube

To evaluate the effect of the PSAR tube presence on the airflow and particle delivery, the geometry and mesh of the pulmonary airway with a PSAR tube for the left lung segments was constructed (see Fig. 9(a)). This configuration was determined according to the PSAR tube location shown in Fig. 8(a). Similarly, the PSAR tube for the right lung segments delivery is shown in Fig. 9(b).

The velocity contours in the coronal plane and six cross-sectionals of the pulmonary airways with left and right PSAR tubes are shown in Fig. 10. The areas near the cross-section A-A' in Fig. 10(a) and (b) have been enlarged to visualize the effect of the PSAR tube on the airflow field. The PSAR tube generates boundary layer flows surrounding both inside and outside the tube. The presence of the PSAR tube would reduce the flow rate in the airway, if the pressure drops between the airway inlet and outlets remained unchanged. Also, considering that the particles released from the point source should be driven by an external device, the pressure at the PSAR tube inlet was slightly increased by 3.17 Pa. This setup ensured that the flow rate was maintained at 15 L/min, which is the same as the tube-free cases. However, the change in the velocity distribution of the airway with the PSAR tube downstream of the airway (see cross-sections B-B′ and C-C′) is negligible compared with Fig. 5. The inhalation flow rates of the different lung segments (i.e., SALS, MALS, and ULS) without and with the PSAR tube are summarized in Table 4. The largest relative change of the flow rate is 0.216% in MALS after inserting the PSAR tube. Therefore, the presence of the PSAR tube has negligible effect on the downstream airflow. Nevertheless, the change in the local airflow near the cross-section A-A' (see the red dashed box in Fig. 10) would change the trajectories of the particles and subsequently alter the deposition locations of the particles.

4.7. Effect of the PSAR tube on the DEs of the particles

Fig. 11 shows the effect of the PSAR tube on the DEs of particles with different diameters, i.e., 1 μm, 2.5 μm, 5 μm, and 7.5 μm. The histograms in Fig. 11(a) to (d) visualize the regional DEs of the particles in SALS, MALS, and ULS with and without the PSAR tube. The influence of the PSAR tube on the particle release maps has been also presented at the top of each subfigure in Fig. 11. The random-release cases are also included for comparison. The PSAR-free cases assumed that the particles were ideally released from the circular region as shown in Fig. 8, but the geometry of the PSAR tube was excluded. For the PSAR cases, particles were released from the outlet of the PSAR tube.

In general, the presence of the PSAR tube has a limited effect on the DEs of different lung segments. Taking the delivery of the 2.5 μm particles as an example, the particle release map of the left PSAR tube case (see Fig. 11(b)) has a negligible change compared with the PSAR-free case. The PSAR tube for the left lung increases the DE in SALS from 51.31% to 52.91%, and reduces the DE in MALS from 28.01% to 25.19%. In contrast, the change in the particle release map is noticeable for the targeted delivery to the right lung. A large portion of the particles on the left side of the PSAR tube enters the MALS (see the blue dots of the release map of the right PSAR tube shown in Fig. 11(b)). This results

in an increase in DE of the MALS from 8.85% to 27.23%. However, the DE of SALS decreases from 75.81% to 71.01%.

As the particle diameter increases, the number of deposited particles increases accordingly due to inertial impact. It leads to certain empty spaces in the particle release map (see Fig. 11(c) and (d)). However, the DEs of SALS are similar for particle diameters ranging from 1 to 7.5 μm in Fig. 11(a) to (d). The largest variation in the DEs of SALS is less than 7.12% between the cases with or without the PSAR tube.

For a realizable particle size range, e.g., 1 μm to 7.5 μm, the PSAR approach with optimized PSAR tube location can at least increase the DE of the SALS by a factor of 3.2× higher than conventional non-targeted drug aerosol inhalation. In addition, this approach could be predicted without considering the geometry of the PSAR tube. Therefore, it enables a relatively rapid assessment for the drug-aerosol delivery targeting specific lung segments.

The completion of the simulation pipeline can be done in 24 h. The whole process includes the one-way coupled simulations of air-particle flow, plotting of the release maps of particles with different diameters, and optimization of the location of the PSAR tube, if the standard for the mesh generation, e.g., cell size and layers of mesh of boundary layer, is determined. 3D printing a biocompatible endotracheal tube including the PSAR tube may take only a few hours [73]. Thus, this in silico method is time effective and could be utilized to design a patient-specific treatment plan, which may prevent the deterioration in moderate patients with COVID-19 in time.

Furthermore, it is ready to be extended for other targeted drug-aerosol delivery applications, e.g., inhalation therapy to treat lung cancer [52,53].

5. Conclusions

In this study, CFD simulations are performed to predict airflow and drug particles transport and deposition in a patient-specific TB tree with moderate COVID-19. Targeted drug delivery has been analyzed and achieved at an inhalation flow rate of 15 L/min. The point-source aerosol release (PSAR) approach is proposed and evaluated to achieve the targeted drug delivery to the severely affected lung segments (SALS) induced by SARS-CoV-2 infection. The optimal PSAR tube location was determined by an in-house customized C++ program which analyzed the CFD simulation results. Effects of the presence of the PSAR tube on particle release map and particle delivery efficiency (DE) in SALS have been investigated. Key conclusions are summarized below, i.e.,

(1) For a realizable particle size range (i.e., 1 μm to 7.5 μm), the change in the optimized particle-release location to the SALS is limited at a flow rate of 15 L/min. This indicates that segment-specific targeted delivery of drug therapy is feasible.
(2) The PSAR approach can at least increase the DE of the SALS 3.2 times higher than the conventional random-release approach for drug-aerosol inhalation.
(3) The presence of the PSAR tube at the inlet only causes 7.12% decrease in DEs in SALS. Thus, the PSAR approach could be rapidly assessed for the drug aerosol delivery targeting specific lung segments without creating the PSAR tube geometry and mesh for the simulation.

Data availability

The data that support the findings of this study are available from the corresponding author upon reasonable request.

Declaration of Competing Interest

The authors declare that they have no known competing financial interests or personal relationships that could have appeared to influence the work reported in this paper.

Acknowledgment

References

[1] A. Bernheim, X.Y. Mei, M.Q. Huang, Y. Yang, Z.A. Fayad, N. Zhang, K.Y. Diao, B. Lin, X.Q. Zhu, K.W. Li, S.L. Li, H. Shan, A. Jacobi, M. Chung, Chest CT findings in coronavirus disease 2019 (COVID-19): relationship to duration of infection, Radiology. 295 (2020) 685–691, https://doi.org/10.1148/radiol.2020200463.

[2] W.J. Guan, Z.Y. Ni, Y. Hu, W.H. Liang, N.S. Zhong, Clinical characteristics of coronavirus disease 2019 in China, N. Engl. J. Med. 382 (2020) 1708–1720, https://doi.org/10.1056/NEJMoa2002032.

[3] M.G. Ahamad, F. Tanin, B. Talukder, M.U. Ahmed, Officially confirmed COVID-19 and unreported COVID-19-like illness death counts: an assessment of reporting discrepancy in Bangladesh, Am. J. Trop. Med. Hyg. 140 (2021) 546–548, https://doi.org/10.4269/ajtmh.20-1205.

[4] S.H. Jacobson, J.A. Jokela, Beyond COVID-19 deaths during the COVID-19 pandemic in the United States, Health Care Manag. Sci. 24 (2021) 661–665, https://doi.org/10.1007/s10729-021-09570-4.

[5] S. Gupta, J. Cantor, K.I. Simon, A.I. Bento, C. Wing, C.M. Whaley, Vaccinations against COVID-19 may have averted up to 140,000 deaths in the United States, Health Aff. 40 (2021) 1465–1472, https://doi.org/10.1377/hlthaff.2021.00619.

[6] WHO, WHO Coronavirus (COVID-19) Dashboard, https://covid19.who.int/ 2021 (accessed 20 December 2021).

[7] R. Dhand, M. Dolovich, B. Chipps, T.R. Myers, R. Restrepo, J.R. Farrar, The role of nebulized therapy in the management of COPD: evidence and recommendations, COPD. 9 (2012) 58–72, https://doi.org/10.3109/15412555.2011.630047.

[8] M. Bonini, O.S. Usmani, The importance of inhaler devices in the treatment of COPD, COPD Res. Pract. 1 (2015) 9, https://doi.org/10.1186/s40749-015-0011-0.

[9] J.L. Rau, The inhalation of drugs: advantages and problems, Respir. Care 50 (2005) 367–382, http://rc.rcjournal.com/content/50/3/367.

[10] B.B. Eedara, W. Alabsi, D. Encinas-Basurto, R. Polt, J.G. Ledford, H.M. Mansour, Inhalation delivery for the treatment and prevention of COVID-19 infection, Pharmaceutics. 13 (2021) 1077, https://doi.org/10.3390/pharmaceutics13071077.

[11] A.A.H. Abdellatif, H.M. Tawfeek, A. Abdelfattah, G. El-Saber Batiha, H.F. Hetta, Recent updates in COVID-19 with emphasis on inhalation therapeutics: nanostructured and targeting systems, J. Drug Deliv. Sci. Technol. 63 (2021) 102435, https://doi.org/10.1016/j.jddst.2021.102435.

[12] F.M.P. van Haren, C. Page, J.G. Laffey, A. Artigas, M. Camprubi-Rimblas, Q. Nunes, R. Smith, J. Shute, M. Carroll, J. Tree, M. Carroll, D. Singh, T. Wilkinson, B. Dixon, Nebulised heparin as a treatment for COVID-19: scientific rationale and a call for randomised evidence, Crit. Care 24 (2020) 454, https://doi.org/10.1186/s13054-020-03148-2.

[13] L.-M. Yu, M. Bafadhel, J. Dorward, G. Hayward, B.R. Saville, O. Gbinigie, O. Van Hecke, E. Ogburn, P.H. Evans, N.P.B. Thomas, M.G. Patel, D. Richards, N. Berry, M.A. Detry, C. Saunders, M. Fitzgerald, V. Harris, M. Shanyinde, S. de Lusignan, M.I. Andersson, P.J. Barnes, R.E.K. Russell, F.D.R. Hobbs, C.C. Butler, L.-M. Yu, M. Bafadhel, J. Dorward, G. Hayward, B.R. Saville, O. Gbinigie, O. van Hecke, E. Ogburn, P.H. Evans, N.P.B. Thomas, M.G. Patel, D. Richards, N. Berry, M.A. Detry, C.T. Saunders, M. Fitzgerald, V. Harris, M. Shanyinde, S. de Lusignan, M.I. Andersson, P.J. Barnes, R.E.K. Russell, D.V. Nicolau, S. Ramakrishnan, F.D.R. Hobbs, C.C. Butler, Inhaled budesonide for COVID-19 in people at high risk of complications in the community in the UK (PRINCIPLE): a randomised, controlled, open-label, adaptive platform trial, Lancet. 398 (2021) 843–855, https://doi.org/10.1016/s0140-6736(21)01744-x.

[14] S. Sahakijpijarn, C. Moon, Z.N. Warnken, E.Y. Maier, J.E. DeVore, D.J. Christensen, J.J. Koleng, R.O. Williams 3rd, In vivo pharmacokinetic study of remdesivir dry powder for inhalation in hamsters, Int. J. Pharm. 3 (2021) 100073, https://doi.org/10.1016/j.ijpx.2021.100073.

[15] K. Li, J. Wu, F. Wu, D. Guo, L. Chen, Z. Fang, C. Li, The clinical and chest CT features associated with severe and critical COVID-19 pneumonia, Investig. Radiol. 55 (2020) 327–331, https://doi.org/10.1097/RLI.0000000000000672.

[16] S.P. Conway, K.G. Brownlee, M. Denton, D.G. Peckham, Antibiotic treatment of multidrug-resistant organisms in cystic fibrosis, Am. J. Respir. Med. 2 (2003) 321–332, https://doi.org/10.1007/BF03256660.

[17] R.W. Johnstone, A.A. Ruefli, S.W. Lowe, Apoptosis: a link between cancer genetics and chemotherapy, Cell. 108 (2002) 153–164, https://doi.org/10.1016/s0092-8674(02)00625-6.

[18] C. Kleinstreuer, Z. Zhang, J.F. Donohue, Targeted drug-aerosol delivery in the human respiratory system, Annu. Rev. Biomed. Eng. 10 (2008) 195–220, https://doi.org/10.1146/annurev.bioeng.10.061807.160544.

[19] N.R. Labiris, M.B. Dolovich, Pulmonary drug delivery. Part I: Physiological factors affecting therapeutic effectiveness of aerosolized medications, Brit. J. Clin. Pharmacol. 56 (2003) 588–599, https://doi.org/10.1046/j.1365-2125.2003.01892.x.

[20] B. Sul, A. Wallqvist, M.J. Morris, J. Reifman, V. Rakesh, A computational study of the respiratory airflow characteristics in normal and obstructed human airways, Comput. Biol. Med. 52 (2014) 130–143, https://doi.org/10.1016/j.compbiomed.2014.06.008.

[21] A. Ernst, D. Feller-Kopman, H.D. Becker, A.C. Mehta, Central airway obstruction, Am. J. Respir. Crit. Care Med. 169 (2004) 1278–1297, https://doi.org/10.1164/rccm.200210-1181SO.

[22] G.A. Otterson, M.A. Villalona-Calero, S. Sharma, M.G. Kris, A. Imondi, M. Gerber, D.A. White, M.J. Ratain, J.H. Schiller, A. Sandler, M. Kraut, S. Mani, J.R. Murren, Phase I study of inhaled doxorubicin for patients with metastatic tumors to the lungs, Clin. Cancer Res. 13 (2007) 1246–1252, https://doi.org/10.1158/1078-0432.CCR-06-1096.

[23] J.S. Patton, P.R. Byron, Inhaling medicines: delivering drugs to the body through the lungs, Nat. Rev. Drug Discov. 6 (2007) 67–74, https://doi.org/10.1038/nrd2153.

[24] M.A. Dolovich, Influence of inspiratory flow rate, particle size, and airway caliber on aerosolized drug delivery to the lung, Respir. Care 45 (2000) 597–608 https://europepmc.org/article/med/10894453.

[25] K.L. Zeman, J.H. Wu, W.D. Bennett, Targeting aerosolized drugs to the conducting airways using very large particles and extremely sow inhalations, J. Aerosol. Med. Pulm. Deliv. 23 (2010) 363–369, https://doi.org/10.1089/jamp.2008.0711.

[26] C. Darquenne, J.S. Fleming, I. Katz, A.R. Martin, J. Schroeter, O.S. Usmani, J. Venegas, O. Schmid, Bridging the gap between science and clinical efficacy: physiology, imaging, and modeling of aerosols in the lung, J. Aerosol. Med. Pulm. Deliv. 29 (2016) 107–126, https://doi.org/10.1089/jamp.2015.1270.

[27] W.H. Finlay, The Mechanics of Inhaled Pharmaceutical Aerosols, New York, 2001.

[28] Z.B. Tong, B. Zheng, R.Y. Yang, A.B. Yu, H.K. Chan, CFD-DEM investigation of the dispersion mechanisms in commercial dry powder inhalers, Powder Technol. 240 (2013) 19–24, https://doi.org/10.1016/j.powtec.2012.07.012.

[29] R. Ponzini, R. Da Vià, S. Bnà, C. Cottini, A. Benassi, Coupled CFD-DEM model for dry powder inhalers simulation: validation and sensitivity analysis for the main model parameters, Powder Technol. 385 (2021) 199–226, https://doi.org/10.1016/j.powtec.2021.02.044.

[30] T. Suwandecha, W. Wongpoowarak, K. Maliwan, T. Srichana, Effect of turbulent kinetic energy on dry powder inhaler performance, Powder Technol. 267 (2014) 381–391, https://doi.org/10.1016/j.powtec.2014.07.044.

[31] R. Han, G. Papadopoulos, B.J. Greenspan, Investigation of powder dispersion inside a SPIROS (R) dry dry powder inhaler using particle image velocimetry, Powder Technol. 125 (2002) 266–278, https://doi.org/10.1016/S0032-5910(01)00515-0.

[32] A.R. Martin, W.H. Finlay, Enhanced deposition of high aspect ratio aerosols in small airway bifurcations using magnetic field alignment, J. Aerosol Sci. 39 (2008) 679–690, https://doi.org/10.1016/j.jaerosci.2008.04.003.

[33] G.E.S. Redman, A.R. Martin, P. Waszak, R.B. Thompson, P.-Y. Cheung, B. Thébaud, W.H. Finlay, Pilot study of inhaled aerosols targeted via magnetic alignment of high aspect ratio particles in rabbits, J. Nanomater. 2011 (2011) 130721, https://doi.org/10.1155/2011/130721.

[34] C. Kleinstreuer, Z. Zhang, Z. Li, W.L. Roberts, C. Rojas, A new methodology for targeting drug-aerosols in the human respiratory system, Int. J. Heat Mass Transf. 51 (2008) 5578–5589, https://doi.org/10.1016/j.ijheatmasstransfer.2008.04.052.

[35] M. Yousefi, K. Inthavong, J. Tu, Microparticle transport and deposition in the human oral airway: toward the smart spacer, Aerosol Sci. Technol. 49 (2015) 1109–1120, https://doi.org/10.1080/02786826.2015.1101052.

[36] M. Hindle, P.W. Longest, Evaluation of enhanced condensational growth (ECG) for controlled respiratory drug delivery in a mouth-throat and upper tracheobronchial model, Pharmacol. Res. 27 (2010) 1800–1811, https://doi.org/10.1007/s11095-010-0165-z.

[37] Z. Li, C. Kleinstreuer, Z. Zhang, Particle deposition in the human tracheobronchial airways due to transient inspiratory flow patterns, J. Aerosol Sci. 38 (2007) 625–644, https://doi.org/10.1016/j.jaerosci.2007.03.010.

[38] C. Kleinstreuer, Z. Zhang, Z. Li, Modeling airflow and particle transport/deposition in pulmonary airways, Respir. Physiol. Neurobiol. 163 (2008) 128–138, https://doi.org/10.1016/j.resp.2008.07.002.

[39] W. Yan, C. Tang, Y. Liu, G. Li, Numerical study on abnormal airflow patterns and particle deposition characteristics in the realistic HUA model with pharyngeal obstruction, Powder Technol. 356 (2019) 148–161, https://doi.org/10.1016/j.powtec.2019.08.007.

[40] F. Huang, Y. Zhang, Z.B. Tong, X.L. Chen, R.Y. Yang, A.B. Yu, Numerical investigation of deposition mechanism in three mouth–throat models, Powder Technol. 378 (2021) 724–735, https://doi.org/10.1016/j.powtec.2018.11.095.

[41] X. Zheng, R. Mittal, Q. Xue, S. Bielamowicz, Direct-numerical simulation of the glottal jet and vocal-fold dynamics in a three-dimensional laryngeal model, J. Acoust. Soc. Am. 130 (2011) 404–415, https://doi.org/10.1121/1.3592216.

[42] J. Zhao, Y. Feng, C.A. Fromen, Glottis motion effects on the particle transport and deposition in a subject-specific mouth-to-trachea model: a CFPD study, Comput. Biol. Med. 116 (2020), 103532 https://doi.org/10.1016/j.compbiomed.2019.103532.

[43] Y. Feng, X. Chen, M. Yang, An in silico investigation of a lobe-specific targeted pulmonary drug delivery method, Design of Medical Devices Conference, 2018. https://doi.org/10.1115/DMD2018-6928.

[44] M.S. Islam, P. Larpruenrudee, A.R. Paul, G. Paul, T. Gemci, Y. Gu, S.C. Saha, SARS CoV-2 aerosol: how far it can travel to the lower airways? Phys. Fluids 33 (2021) 061903, https://doi.org/10.1063/5.0053351.

[45] A. Tiwari, A. Jain, A.R. Paul, S.C. Saha, Computational evaluation of drug delivery in human respiratory tract under realistic inhalation, Phys. Fluids 33 (2021) 083311, https://doi.org/10.1063/5.0053980.

[46] J.S. Patton, C.S. Fishburn, J.G. Weers, The lungs as a portal of entry for systemic drug delivery, Proc. Am. Thorac. Soc. 1 (2004) 338–344, https://doi.org/10.1513/pats.200409-049TA.

[47] C.A. Cox, A.B. Cullen, M.R. Wolfson, T.H. Shaffer, Intratracheal administration of perfluorochemical-gentamicin suspension: a comparison to intravenous administration in normal and injured lungs, Pediatr. Pulmonol. 32 (2001) 142–151, https://doi.org/10.1002/ppul.1100.abs.

[48] J. Kim, J.D. O'Neill, N.V. Dorrello, M. Bacchetta, G. Vunjak-Novakovic, Targeted delivery of liquid microvolumes into the lung, P Natl. Acad. Sci. USA. 112 (2015) 11530–11535, https://doi.org/10.1073/pnas.1512613112.

[49] K. Selting, J.C. Waldrep, C. Reinero, K. Branson, D. Gustafson, D.Y. Kim, C. Henry, N. Owen, R. Madsen, R. Dhand, Feasibility and safety of targeted cisplatin delivery to a select lung lobe in dogs via the AeroProbe intracorporeal nebulization catheter, J. Aerosol. Med. Pulm. Deliv. 21 (2008) 255–268, https://doi.org/10.1089/jamp.2008.0684.

[50] K. Selting, S. Essman, C. Reinero, K.R. Branson, C.J. Henry, N. Owen, V.P. Guntur, J.C. Waldrep, D.Y. Kim, R. Dhand, Targeted combined aerosol chemotherapy in dogs and radiologic toxicity grading, J. Aerosol. Med. Pulm. Deliv. 24 (2011) 43–48, https://doi.org/10.1089/jamp.2010.0822.

[51] E.L. Kolewe, Y. Feng, C.A. Fromen, Realizing lobe-specific aerosol targeting in a 3D-printed in vitro lung model, J. Aerosol. Med. Pulm. Deliv. 34 (2021) 42–56, https://doi.org/10.1089/jamp.2019.1564.

[52] H.M. Abdelaziz, M. Gaber, M.M. Abd-Elwakil, M.T. Mabrouk, M.M. Elgohary, N.M. Kamel, D.M. Kabary, M.S. Freag, M.W. Samaha, S.M. Mortada, K.A. Elkhodairy, J.Y. Fang, A.O. Elzoghby, Inhalable particulate drug delivery systems for lung cancer therapy: nanoparticles, microparticles, nanocomposites and nanoaggregates, J. Control. Release 269 (2018) 374–392, https://doi.org/10.1016/j.jconrel.2017.11.036.

[53] N. Alhajj, C.F. Chee, T.W. Wong, N.A. Rahman, N.H. Abu Kasim, P. Colombo, Lung cancer: active therapeutic targeting and inhalational nanoproduct design, Expert Opin. Drug Deliv. 15 (2018) 1223–1247, https://doi.org/10.1080/17425247.2018.1547280.

[54] C. Darquenne, Aerosol deposition in health and disease, J. Aerosol. Med. Pulm. Deliv. 25 (2012) 140–147, https://doi.org/10.1089/jamp.2011.0916.

[55] C. Kleinstreuer, Z. Zhang, C.S. Kim, Combined inertial and gravitational deposition of microparticles in small model airways of a human respiratory system, J. Aerosol Sci. 38 (2007) 1047–1061, https://doi.org/10.1016/j.jaerosci.2007.08.010.

[56] S.A. Morsi, A.J. Alexander, An investigation of particle trajectories in two-phase flow systems, J. Fluid Mech. 55 (1972) 193–208, https://doi.org/10.1017/s0022112072001806.

[57] Z. Zhang, C. Kleinstreuer, J.F. Donohue, C.S. Kim, Comparison of micro- and nano-size particle depositions in a human upper airway model, J. Aerosol Sci. 36 (2004) 211–233, https://doi.org/10.1016/j.jaerosci.2004.08.006.

[58] Hinds, Aerosol Technology: Properties, Behavior, and Measurement of Airborne Particles, New York, 1982.

[59] C.S. Kim, D.M. Fisher, Deposition characteristics of aerosol particles in sequentially bifurcating airway models, Aerosol Sci. Technol. 31 (1999) 198–220, https://doi.org/10.1080/027868299304255.

[60] L.L.X. Augusto, J.A.S. Gonçalves, G.C. Lopes, CFD evaluation of the influence of physical mechanisms, particle size, and breathing condition on the deposition of particulates in a triple bifurcation airway, Water Air Soil Pollut. 227 (2016) 56, https://doi.org/10.1007/s11270-016-2753-y.

[61] Y.H. Kim, Z.B. Tong, H.K. Chan, R.Y. Yang, CFD modelling of air and particle flows in different airway models, J. Aerosol Sci. 134 (2019) 14–28, https://doi.org/10.1016/j.jaerosci.2019.04.015.

[62] X. Chen, W. Zhong, B. Sun, B. Jin, X. Zhou, Study on gas/solid flow in an obstructed pulmonary airway with transient flow based on CFD–DPM approach, Powder Technol. 217 (2012) 252–260, https://doi.org/10.1016/j.powtec.2011.10.034.

[63] X. Chen, W. Zhong, X. Zhou, B. Jin, B. Sun, CFD-DEM simulation of particle transport and deposition in pulmonary airway, Powder Technol. 228 (2012) 309–318, https://doi.org/10.1016/j.powtec.2012.05.041.

[64] X. Chen, Y. Feng, W. Zhong, B. Sun, F. Tao, Numerical investigation of particle deposition in a triple bifurcation airway due to gravitational sedimentation and inertial impaction, Powder Technol. 323 (2018) 284–293, https://doi.org/10.1016/j.powtec.2017.09.050.

[65] Y. Feng, J. Zhao, X. Chen, J. Lin, An in silico subject-variability study of upper airway morphological influence on the airflow regime in a tracheobronchial tree, Bioengineering. 4 (2017) 90, https://doi.org/10.3390/bioengineering4040090.

[66] W. Hofmann, Modelling inhaled particle deposition in the human lung—a review, J. Aerosol Sci. 42 (2011) 693–724, https://doi.org/10.1016/j.jaerosci.2011.05.007.

[67] Z. Zhang, C. Kleinstreuer, C.S. Kim, Cyclic micron-size particle inhalation and deposition in a triple bifurcation lung airway model, J. Aerosol Sci. 33 (2002) 257–281, https://doi.org/10.1016/s0021-8502(01)00170-7.

[68] L. Nicolaou, Inertial and gravitational effects on aerosol deposition in the conducting airways, J. Aerosol Sci. 120 (2018) 32–51, https://doi.org/10.1016/j.jaerosci.2018.03.003.

[69] H. Shi, C. Kleinstreuer, Z. Zhang, C.S. Kim, Nanoparticle transport and deposition in bifurcating tubes with different inlet conditions, Phys. Fluids 16 (2004) 2199–2213, https://doi.org/10.1063/1.1724830.

[70] Z. Zhang, C. Kleinstreuer, C.S. Kim, Flow structure and particle transport in a triple bifurcation airway model, J. Fluid Eng. T ASME 123 (2001) 320–330, https://doi.org/10.1115/1.1359525.

[71] Z. Zhang, C. Kleinstreuer, C.S. Kim, Gas–solid two-phase flow in a triple bifurcation lung airway model, Int. J. Multiphase Flow 28 (2002) 1021–1046, https://doi.org/10.1016/S0301-9322(02)00011-3.

[72] Y. Feng, C. Kleinstreuer, Micron-particle transport, interactions and deposition in triple lung-airway bifurcations using a novel modeling approach, J. Aerosol Sci. 71 (2014) 1–15, https://doi.org/10.1016/j.jaerosci.2014.01.003.

[73] N. Anandakrishnan, H. Ye, Z. Guo, Z. Chen, K.I. Mentkowski, J.K. Lang, N. Rajabian, S.T. Andreadis, Z. Ma, J.A. Spernyak, J.F. Lovell, D. Wang, J. Xia, C. Zhou, R. Zhao, Fast stereolithography printing of large-scale biocompatible hydrogel models, Adv. Healthc. Mater. 10 (2021) 2002103, https://doi.org/10.1002/adhm.202002103.